DOI: 10.1002/zaac.201000028

Structural Effects of Cu/Zn Substitution in the Malachite–Rosasite System

Malte Behrens*[a] and Frank Girgsdies[a]

Dedicated to Professor Rüdiger Kniep on the Occasion of His 65th Birthday

Keywords: Malachite; Rosasite; Jahn–Teller distortion; Copper; Zinc; Heterogeneous catalysis

Abstract. Synthetic zincian malachite samples $(Cu_{1-x}Zn_x)_2(OH)_2CO_3$ with x = 0, 0.1, 0.2 and 0.3 were characterized by powder X-ray diffraction and optical spectroscopy. The XRD patterns of the samples up to x = 0.2 indicate single phase materials with an approximately linear dependence of the refined lattice parameters on the zinc content. In contrast, the sample with a nominal zinc content x = 0.3 shows the formation of a small amount of aurichalcite $(Zn,Cu)_5(OH)_6(CO_3)_2$ as an additional phase. Based on the lattice parameter variations, the zinc content of the zincian malachite component in this sample is estimated to be $x \approx 0.27$, which seems to represent the maximum possible substitution in zincian malachite under the synthesis conditions applied. The results are discussed in relation to preparation of Cu/ZnO catalysts and the crystal structures of the minerals malachite and rosasite. One striking difference between these two structurally closely related phases is the orientation of the Jahn–Teller elongated axes of the CuO_6 octahedra in the unit cell, which seems to be correlated with the placement of the monoclinic β angle. The structural and chemical relationship between these crystallographically distinct phases is discussed using a hypothetical intermediate $Zn_2(OH)_2CO_3$ phase of higher orthorhombic symmetry. In addition to the crystallographic analysis, optical spectroscopy proves to be a useful tool for estimation of the Cu:Zn ratio in $(Cu_{1-x}Zn_x)_2(OH)_2CO_3$ samples.

Introduction

Rosasite is a mineral of the chemical composition $(Cu_{1-x}Zn_x)_2(OH)_2CO_3$ with approximately $0.3 < x < 0.5$. The related pure copper mineral, $Cu_2(OH)_2CO_3$, is malachite whose monoclinic crystal structure is reported in the literature [1]. Whereas synthetic malachite can be easily prepared by precipitation, synthetic rosasite samples, i.e. single phase compounds with $x > 0.3$, are much harder to obtain, because usually aurichalcite, $(Cu_{1-x}Zn_x)_5(OH)_6(CO_3)_2$ with $x > 0.5$, is formed if zinc-rich solutions are used for coprecipitation [2]. The cell parameters and space group of rosasite were reported in [3] and atomic coordinates were recently revealed on the basis of powder diffraction studies [4]. Both malachite and rosasite are monoclinc, space group $P2_1/a$ (No. 14), crystallize in different crystal structures and are, thus, not isomorphous despite their similar compositions. However, the close relation of the two phases is apparent from the similar powder diffraction patterns (Figure 1) and was recently discussed by *Perchiazzi* [4, 5]. It is interesting to note that rosasite analogous minerals were found also with magnesium, nickel or cobalt instead of zinc together forming the rosasite group of minerals.

These mixed basic transition metal carbonates have not only attracted the attention of mineralogists, but also of solid state chemists active in the field of heterogeneous catalysis, because $(Cu_{1-x}Zn_x)(OH)_2CO_3$ is the relevant precursor compound for the preparation of nanostructured Cu/ZnO catalysts [6–9]. Such catalysts are employed in industrial synthesis of methanol from syngas, one of the top ten chemical processes worldwide. A highly substituted synthetic rosasite-like precursor would be

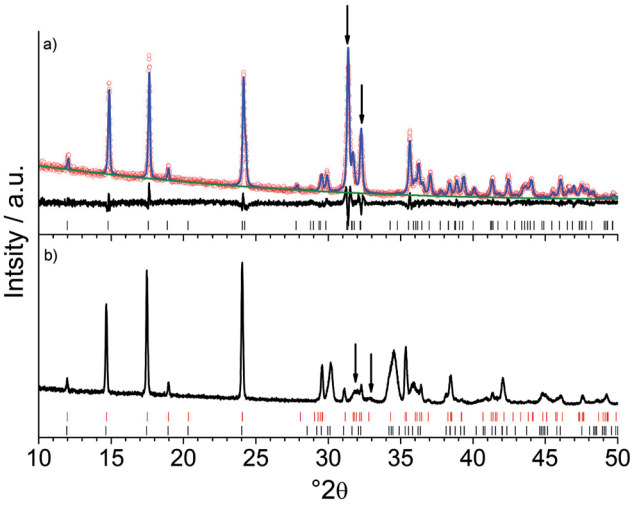

Figure 1. Sections of the experimental and calculated powder XRD patterns of a natural sample of malachite (a) (dots: experimental data, blue line: calculated pattern, green line: background, bottom curve: difference plot, ticks: peak positions). Sections of the experimental pattern and refined peak positions (red ticks: malachite, black ticks: rosasite) of the rosasite sample (b). The $(20\bar{1})$ and $(21\bar{1})$ reflections of malachite are marked.

* Dr. M. Behrens
Fax: +49-30-8413-4405
E-Mail: behrens@fhi-berlin.mpg.de
[a] Fritz-Haber-Institut der Max-Planck-Gesellschaft
Abteilung Anorganische Chemie
Faradayweg 4–6
14195 Berlin, Germany

desirable for catalyst preparation, because the resulting Cu/ZnO material after calcination and reduction is expected to exhibit a higher dispersion of the catalytically active copper phase. This is because the stabilizing function of the ZnO phase in the composite catalyst is more efficient, if large amounts of zinc were homogenously distributed in the cation lattice of the precursor (Figure 2) [6]. However, preparation of $(Cu_{1-x}Zn_x)(OH)_2CO_3$ with substitution levels near $x = 0.5$, i.e. as high as in natural rosasite, remains a challenge and values around $x = 0.3$ cannot be exceeded for state-of-the-art catalysts synthesized from malachite/rosasite-like precursors. Zn-richer aurichalcite precursors were shown to lead to inferior catalysts because aurichalcite is usually obtained in form of large platelets exhibiting an unfavorable *meso*-structure compared to the needle-like zincian malachite.

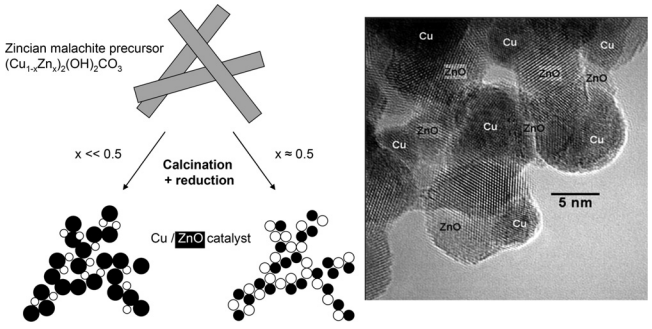

Figure 2. Cartoon of precursor nano-structuring upon thermal treatment (calcination and reduction) during Cu/ZnO catalyst synthesis: Needle-like $(Cu_{1-x}Zn_x)_2(OH)_2CO_3$ crystals decompose and de-mix into copper and ZnO resulting in a nano-particulate Cu/ZnO composite [6], which is shown as HRTEM image for a catalyst with a Cu:Zn ratio of 70:30 [25]. Nano-structuring is more efficient at x near 0.5.

We have started to investigate the structural properties of mixed basic Cu,Zn carbonates from the perspective of Cu/ZnO catalyst preparation and first results have been reported recently [2, 6]. Here, we report on the effects of copper by zinc substitution on the crystal structure and optical absorption properties of malachite and discuss the relationship between synthetic $(Cu_{1-x}Zn_x)(OH)_2CO_3$ and to natural samples of malachite and rosasite.

Results and Discussion

A comparison of the crystal structures of natural malachite [1] and rosasite [4] based on literature data, is shown in Figure 3. The main building blocks are $(Cu,Zn)O_6$ octahedra and two distinct metal sites are present in both structures (Table 1). As pointed out by *Perchiazzi* [4], the view along the *c*-axis (Figure 3, top row) shows equal connectivity of the octahedral units in both minerals in form of "double ribbons" of two edge-sharing octahedra running along [001]. The major structural difference of the two phases becomes apparent if the view is slightly tilted towards the (110) plane (Figure 3, bottom row), showing that the monoclinic angle is placed between the short and the medium axes in malachite but between the short and the long axes in rosasite. Thus, one might get the idea that both in malachite and rosasite the monoclinic angle β is shifted towards 90° as the Cu:Zn ratio changes and that a hypothetical orthorhombic parent structure exists for both minerals, possibly at an intermediate value of x.

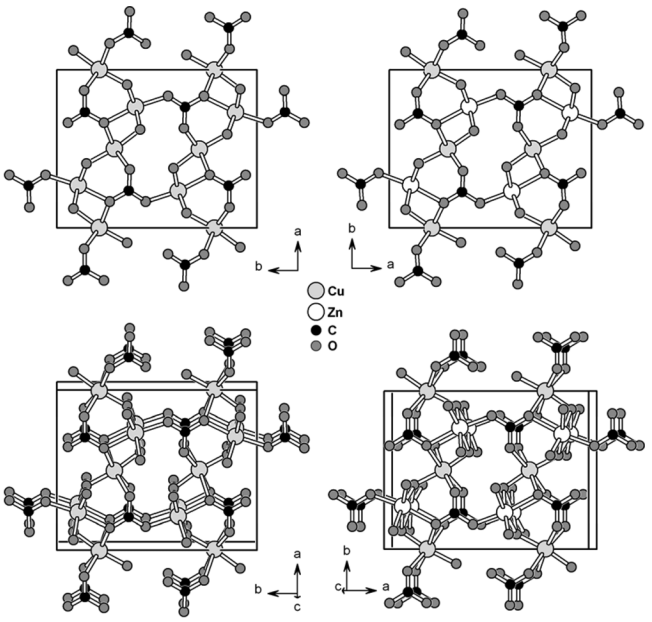

Figure 3. Comparison of the crystal structures of malachite (left) and rosasite (right). A view along the [001] direction (top row) emphasizes their close relationship, whereas a slight change of the viewing angle onto the (001) plane reveals the different placement of the monoclinic angles (bottom row).

The effects of substitution of copper by zinc on the crystal structure of synthetic malachite, leading to zincian malachite, $(Cu_{1-x}Zn_x)(OH)_2CO_3$, were first investigated in detail by *Porta* et al. in 1988 [10, 11]. The authors report a contraction of the unit cell and a systematic shift for the *h*0*l* and *hkl* reflections. We have recently reported a characteristic and very pronounced shift of the $(20\bar{1})$ and $(21\bar{1})$ reflections to higher angles in the XRD patterns as copper is gradually substituted by zinc [2]. The unusual effect on these characteristic XRD peaks was explained as a ligand field effect. In brief, the Jahn–Teller elongated axes of the CuO_6 octahedra in malachite exhibit an orientation nearly perpendicular to either the $(20\bar{1})$ or $(21\bar{1})$ lattice planes (Figure 4). The unit cell is strongly contracted in the directions perpendicular to these planes as the Jahn–Teller ions Cu^{2+} are substituted with Zn^{2+} forming more regular octahedra. Thus, the *d*-spacing of these characteristic reflections can be used as a sensitive indicator for the degree of zinc incorporation in the malachite structure.

It remains, however, puzzling that certain reflections move strongly, whereas others remain more or less fixed (Figure 5) despite their interrelation by the cell parameters. In particular, the intensive XRD peaks below 30° 2θ, which are often used as fingerprint reflections for precursor phase identification in catalysis research, do hardly give information on the Cu:Zn ratio. This could be generally expected from the similar ionic radii of Cu^{2+} and Zn^{2+}, but at the same time the $(20\bar{1})$ and $(21\bar{1})$ peaks in the 2θ-range 31–33° indicate pronounced changes of

Zeitschrift für anorganische und allgemeine Chemie ZAAC Journal of Inorganic and General Chemistry

Table 1. Comparison of structural data of natural malachite and rosasite samples reported in literature and in this study. Our rosasite sample contains rosasite as main phase, but also a minor malachite-like fraction (see text).

	Malachite	Rosasite	Malachite sample	Rosasite sample	
Reference	[1]	[4, 5] [a]	this study	Rosasite this study	Malachite this study
a /Å	9.502	12.2413(2)	9.4988(4)	12.2266(15)	9.443(3)
b /Å	11.974	9.3705(2)	11.9663(5)	9.3617(10)	12.080(4)
c /Å	3.240	3.1612(2)	3.24553(11)	3.1595(3)	3.2037(7)
β /°	98.75	98.730(3)	98.636(2)	98.697(8)	97.358(13)
V /Å^3	364.35	357.90	364.72(3)	357.48(6)	362.46(19)
$M1$–O4 /Å	1.898(1)	1.952(9)	1.910(10)	*n.d.*	*n.d.*
$M1$–O5 /Å	1.911(1)	1.89(1)	1.950(9)	*n.d.*	*n.d.*
$M1$–O1 /Å	1.996(1)	2.078(8)	1.966(11)	*n.d.*	*n.d.*
$M1$–O2 /Å	2.055(1)	2.057(5)	2.154(13)	*n.d.*	*n.d.*
$M1$–O1 /Å	2.509(1)	2.443(7)	2.610(13)	*n.d.*	*n.d.*
$M1$–O2 /Å	2.642(1)	2.519(3)	2.649(15)	*n.d.*	*n.d.*
Δ_{M1}	0.0185	0.0123	0.0196	*n.d.*	*n.d.*
$M2$–O4 /Å	1.918(1)	2.01(1)	1.970(12)	*n.d.*	*n.d.*
$M2$–O5 /Å	1.915(1)	2.07(1)	1.955(11)	*n.d.*	*n.d.*
$M2$–O3 /Å	2.049(1)	2.046(3)	1.952(11)	*n.d.*	*n.d.*
$M2$–O2 /Å	2.115(1)	2.256(3)	2.150(11)	*n.d.*	*n.d.*
$M2$–O5 /Å	2.369(1)	2.251(1)	2.473(13)	*n.d.*	*n.d.*
$M2$–O4 /Å	2.372(1)	2.16(1)	2.428(14)	*n.d.*	*n.d.*
Δ_{M2}	0.0079	0.0044	0.0105	*n.d.*	*n.d.*

a) Bond lengths were taken from reference [4], whereas the cell parameters are based for the transformed unit cell given in [5]; *n.d.* = not determined.

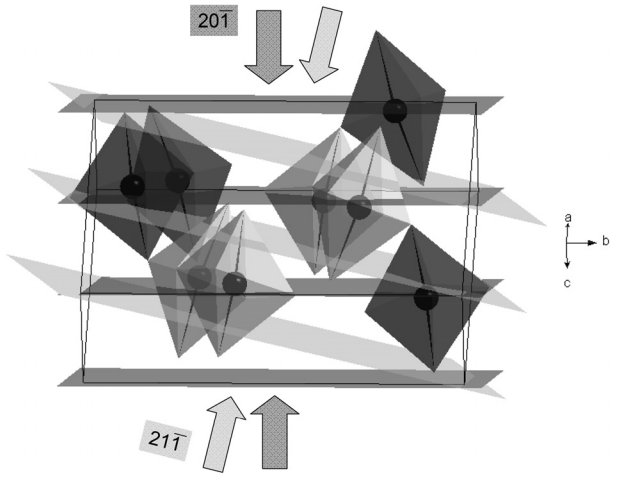

Figure 4. Unit cell of malachite, slightly tilted view towards (50$\bar{1}$). Only the Jahn–Teller elongated bonds of the CuO_6 units are shown. They are oriented either perpendicular to (20$\bar{1}$) (shown in dark grey) or to (21$\bar{1}$) (shown in light grey). The directions of strongest unit cell contraction upon Cu/Zn substitution are indicated by arrows. Carbonate groups were omitted for clarity.

tural model. The samples were synthesized according to established catalyst precursor preparation [12] by coprecipitation and subsequent ageing of the precipitate in the mother liquor, during which crystallization occurs. The Rietveld-fits are graphically shown in Figure 5 and selected results are listed in Table 2. It is noted that the crystallinity of the materials decreased with increasing zinc content. Furthermore, the 70:30 zinc sample contained aurichalcite as an additional phase. For the single phase materials (samples up to $x = 0.2$), a full Rietveld refinement of the atomic coordinates was possible and included in the fitting procedure. In contrast, the poor crystallinity and presence of the aurichalcite by-phase did not allow a reliable refinement of atomic positions for the 70:30 sample. Thus, fixed atomic coordinates as obtained from the fit of the 80:20 sample were used in this case.

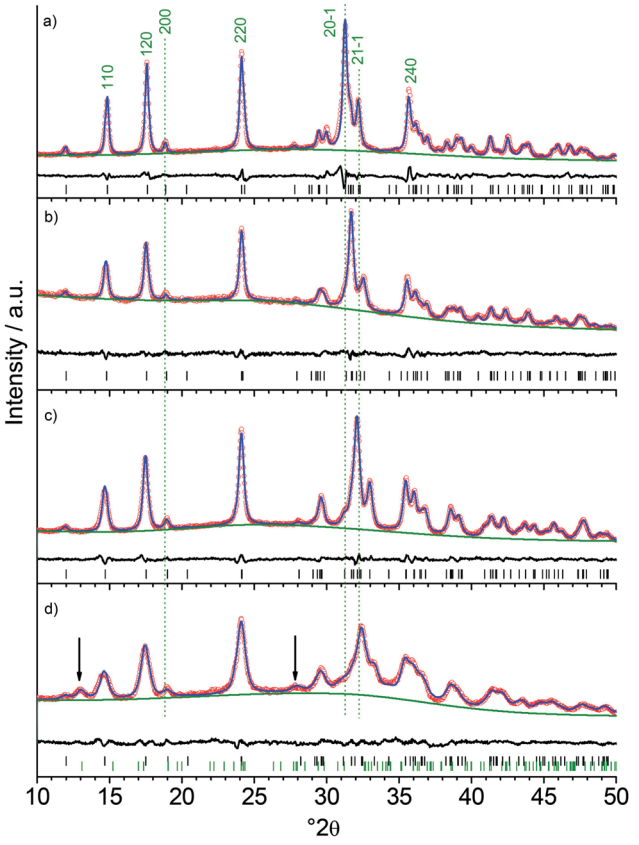

Figure 5. Sections of the experimental and calculated XRD patterns of synthetic zincian malachite with nominal Cu:Zn ratios of 100:0 (a), 90:10 (b), 80:20 (c) and 70:30 (d); the different extent of peak shifts is indicated by vertical lines for selected reflections (dots: experimental data, black line: calculated patterns, grey line: background, bottom curve: difference plot, ticks: peak positions; the two most intensive aurichalcite reflections are marked in (d) and the aurichalcite peak positions are shown in green).

the cell parameters. In addition, the low-angle reflections are not suitable to unambiguously discriminate the malachite and rosasite structures in the mineral phases (Figure 1). This stimulated us to perform full pattern refinements of synthetic zincian malachite samples with nominal molar Cu:Zn ratios of 100:0, 90:10, 80:20 and 70:30 using the mineral malachite as struc-

The unit cell volume and especially the b-axis of the synthetic malachite sample (Table 2) were found to be slightly decreased in comparison to the natural samples (Table 1). The Cu/Zn substitution in malachite leads to a Vegard-type linear trend for all lattice parameters of $(Cu_{1-x}Zn_x)_2(OH)_2CO_3$ in the range $0 < x < 0.2$ (Figure 6). The a- and c-axes, the monoclinic

Table 2. Selected results from the Rietveld refinement of the synthetic zincian malachite samples.

Zn content x	0	0.1	0.2	≈ 0.27
a /Å	9.4938(9)	9.44900(3)	9.4030(7)	9.37228(19)
b /Å	11.9086(11)	11.9749(14)	12.0290(9)	12.060(3)
c /Å	3.2457(3)	3.2198(3)	3.1983(2)	3.1801(5)
β /°	98.684(5)	97.839(6)	96.889(4)	96.190(12)
V /Å^3	362.75(5)	360.92(5)	359.15(4)	357.36(12)
*M*1–O4 /Å	1.914(15)	1.898(15)	1.926(11)	*n.d.*
*M*1–O1 /Å	2.020(16)	1.985(4)	2.017(13)	*n.d.*
*M*1–O5 /Å	2.025(12)	2.057(4)	1.968(11)	*n.d.*
*M*1–O2 /Å	2.097(18)	2.125(5)	2.066(11)	*n.d.*
*M*1–O1 /Å	2.559(18)	2.428(4)	2.404(14)	*n.d.*
*M*1–O2 /Å	2.66(2)	2.786(6)	2.689(14)	*n.d.*
Δ_{M1}	0.0170	0.0190	0.0161	*n.d.*
*M*2–O4 /Å	1.784(18)	1.855(5)	1.841(14)	*n.d.*
*M*2–O5 /Å	1.911(18)	1.954(19)	1.993(13)	*n.d.*
*M*2–O3 /Å	2.078(15)	1.974(9)	2.011(12)	*n.d.*
*M*2–O2 /Å	2.082(15)	2.143(3)	2.087(10)	*n.d.*
*M*2–O5 /Å	2.42(2)	2.47(2)	2.347(14)	*n.d.*
*M*2–O4 /Å	2.51(2)	2.406(5)	2.355(16)	*n.d.*
Δ_{M2}	0.0148	0.0118	0.0080	*n.d.*

n.d. = not determined

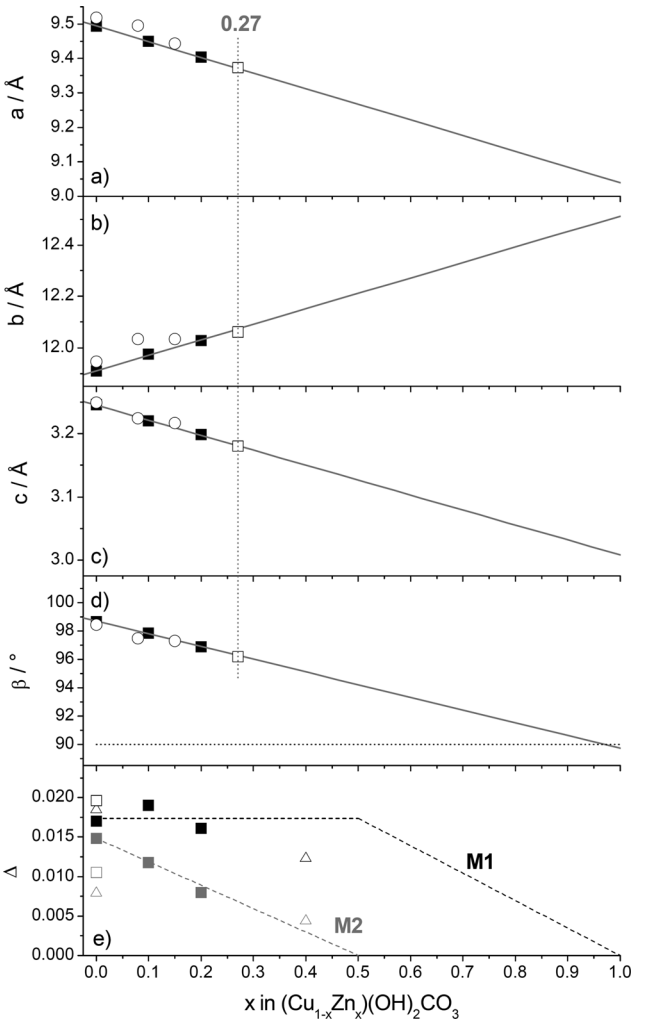

Figure 6. Trends of lattice parameters a (a), b (b), c (c), β (d) and the distortion parameter Δ (e) of synthetic zincian malachite as a function of zinc content. The data represented as circles was taken from [11]. Open symbols in (d) refer to reference data for mineral samples from Table 1 (squares: this study, triangles: literature data of Table 1).

β angle as well as the unit cell volume (Table 2) decrease with increasing zinc content, whereas the b-axis increases. These observations are in line with the results reported by *Porta* et al. [11, 12], who obtained phase pure zincian malachite samples for $x \leq 0.15$. The lattice parameters of their samples are in reasonable agreement with our results and are also shown in Figure 6. It was discussed in [2] that the average contraction of the Jahn–Teller elongated octahedra might be responsible for the cell volume shrinking. The slightly larger ionic radius of Zn^{2+} and the elongation of the equatorial *M*–O bonds are reflected in the increasing b-axis, but obviously do not compensate for the shrinking effect. *Porta* et al. suggested that covalent shortening is responsible for the unit cell volume contraction as the ionic Cu–O bond is substituted by more covalent Zn–O.

Porta et al. also discussed the non-systematic shift of certain groups of reflections [11]. The simultaneous anisotropic change of the lattice parameters causes only minor changes in the XRD patterns, reflected strongly only in the positions of the (20$\bar{1}$) and (21$\bar{1}$) reflections as discussed above. For instance, the shift of the well-resolved (200) reflection near 19° 2θ is only hardly detected in the XRD patterns of the poorly crystalline catalyst precursors (Figure 5), although the a-axis is significantly contracted (Figure 6a). This is because low-angle reflections generally shift less on the angular scale, but also, because the effect of the contracted a-axis (–1.3 % at $x \approx 0.3$) is to some extent compensated by the simultaneous decrease of β leading to smaller changes in the d-spacing of the (h00) planes of only –0.7 %. These peculiarities are summarized in Figure 7 for the six most intensive reflections of zincian malachite showing again the special sensitivity of the (20$\bar{1}$) and (21$\bar{1}$) peaks for the Cu:Zn ratio and the much smaller effect of the structural changes on the other peaks, especially on the angular scale of a conventional Cu-K_α pattern (Figure 7b).

The zinc content of the malachite-like phase fraction in the 70:30 sample was estimated on basis of the linear trends shown in Figure 6. Linear regressions were performed using the first three data points (single phase samples) for all four lattice parameters. The best overall agreement for the lattice parameters of the zincian malachite phase in the fourth sample is obtained when placing it at $x = 0.27$ (Figure 6). This in the range $0.23 < x < 0.33$ suggested by *Porta* et al. on basis of the cell volume contraction [10, 11] and in excellent agreement with the limit of $x = 0.28$ determined from the shift of the (20$\bar{1}$) reflection by single peak fitting in a previous study [2]. It is noted, though, that the values scatter between 0.25 (b-axis) to 0.28 (monoclinic β angle), if the zinc content was estimated for each cell parameter separately.

As laboratory XRD provides no direct access to the distribution of copper and zinc on the two available metal sites in

Zeitschrift für anorganische und allgemeine Chemie ZAAC Journal of Inorganic and General Chemistry

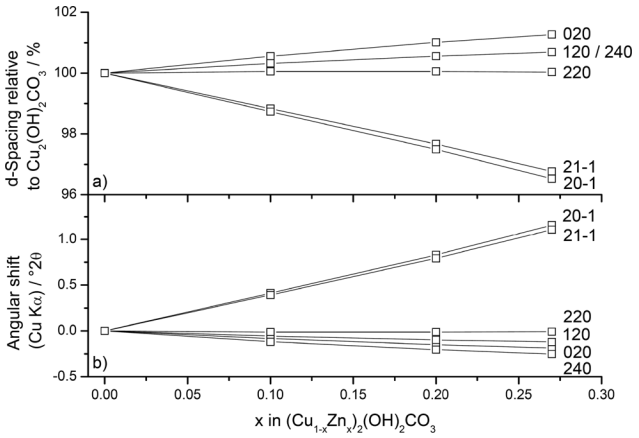

Figure 7. Changes in the powder XRD pattern of zincian malachite samples as a function of zinc content x for the six most intensive reflections.

the malachite structure, the site preference has to be deduced indirectly from the average distortion of the MO$_6$ coordination polyhedra in the structure. Thus, distortion parameters Δ were calculated from the M–O distances d of the $M$1 and $M$2 sites according to $\Delta = (1/6)\Sigma_{n=1,6}\{(d_n - \langle d\rangle)/\langle d\rangle\}^2$, with $\langle d\rangle$ being the average M–O distance and d_n the individual distances (Figure 6e, Table 1, Table 2) [5, 13]. It can be expected that starting from the strongly Jahn–Teller distorted malachite structure, the parameter Δ should decrease for a specific site upon successive substitution of copper with zinc. It can be seen in Figure 6e, that this is the case for the $M$2 site, whereas $M$1 does not show a clear trend. Such a zinc ordering on the $M$2 site is also expected from ligand field considerations, because ($M$2)O$_6$ is the initially less distorted polyhedron in pure malachite (Table 1) and thus more suited for the coordination requirements of Zn^{2+}. The difference between the $M$1 and $M$2 sites is much more pronounced in natural malachite compared to our synthetic material, i.e. the $M$1 site is more distorted and the $M$2 more regular (Figure 6e). This is possibly because a naturally formed mineral should be closer to the thermodynamically favorable site distribution than a synthetic sample, which would be influenced more strongly by randomizing kinetic factors. Consequently, site preference upon Cu/Zn substitution can be expected to be more pronounced in minerals than in synthetic samples. The $M$1:$M$2 ratio in the malachite unit cell is 1:1 and extrapolation of Δ indicates that a hypothetical undistorted ($M$2)O$_6$ is present for zinc contents around $x = 0.5$, suggesting that $M$2 is almost exclusively preferred by zinc also for high substitution levels. This is also in good agreement with the distortion parameters of ($M$2)O$_6$ calculated for natural rosasite (Table 1, Figure 6e) and the site occupancy reported by *Perchiazzi* [4, 5]. However, it should be mentioned in this context that the two $M$2–O bonds in rosasite, which are significantly longer than the remaining four (Table 1), are *cis* to each other, and the resulting distortion Δ is not compatible with the *trans* geometry expected for a Jahn–Teller distorted site.

Coming back to the structural relation of (zincian) malachite and rosasite, indeed an evolution towards 90° is observed for the monoclinic angle β as zinc is incorporated into malachite. However, it is clearly seen in Figure 6d that 90° is not reached at intermediate values of x and that no such orthorhombic parent structure exists in between the regimes of zincian malachite (up to $x \approx 0.3$) and rosasite ($0.3 < x < 0.5$). However, it is interesting to note that the monoclinic angle of malachite indeed becomes 90° as it is extrapolated to $x = 1$ (Figure 6d), suggesting a hypothetical orthorhombic zinc-only phase $Zn_2(OH)_2CO_3$, which to the best of our knowledge has not been reported so far. Following the highly idealized trends shown in Figure 6e as dashed lines, such pure $Zn_2(OH)_2CO_3$ phase can be assumed to consist of relatively regular octahedral building units due to the absence of Cu^{2+}. Starting from malachite, zinc substitution first occurs preferably on the $M$2 site until $x = 0.5$. Beyond this value, the $M$1 site is necessarily filled with Zn^{2+}, leading to successive decrease of the average distortions of the respective octahedra and, in the end, apparently also of the monoclinic distortion of the unit cell. These considerations are highly idealized, because other contributions than Jahn–Teller distortions that may contribute to the monoclinic distortion of the unit cell are neglected. It is noted in this context that the structures of the minerals pokrovskite [5] and chukanovite [14], $M_2(OH)_2CO_3$ with $M = Mg^{2+}$ and Fe^{2+}, respectively, can be refined in the monoclinic rosasite structure type despite the absence of Jahn–Teller ions, suggesting an intrinsic monoclinic distortion of these minerals. Interestingly, a sub-stoichiometric occupation of the cation sites was reported for the former and could not be excluded for the latter mineral.

However, the simplified picture of hypothetical, undistorted, orthorhombic $Zn_2(OH)_2CO_3$ allows an "inverse" gedankenexperiment, in which malachite and rosasite are derived from such common $Zn_2(OH)_2CO_3$ phase as starting material. Assuming Cu/Zn ordering for both phases, the $M$1 site would be gradually filled with Cu^{2+} now introducing Jahn–Teller elongation of given axial $M$1–O bonds in the initially almost undistorted octahedra. In this situation, different possibilities for the orientation of these elongated axes in the unit cell exist, as there is the choice between the three orthogonal fourfold rotation axes of the M1O$_6$ octahedra. This leads to the principal difference of the malachite and the rosasite structure as can be seen in Figure 8 showing both crystal structures along their crystallographic axes. It is noted that because of the different orientation of the monoclinic angles, and according to crystallographic convention, requireing the b-axis to be the monoclinic axis, the a-axis of malachite corresponds to the b-axis of rosasite, and vice versa. Thus, the [010] view of malachite is analogous to the [100] view of rosasite (Figure 8, top row), whereas the structural situation in malachite viewed along [100] is represented in the [010] view of rosasite (Figure 8, center row).

The Jahn–Teller elongated bonds of the CuO$_6$ polyhedra of those metal sites which are mainly occupied by copper ($M$1 and $M$2 in malachite and $M$1 in rosasite) are emphasized in black in Figure 8. It can be seen that, when viewed along the long axes (top row), their projections are aligned almost in parallel in malachite, whereas they exhibit a nearly perpendic-

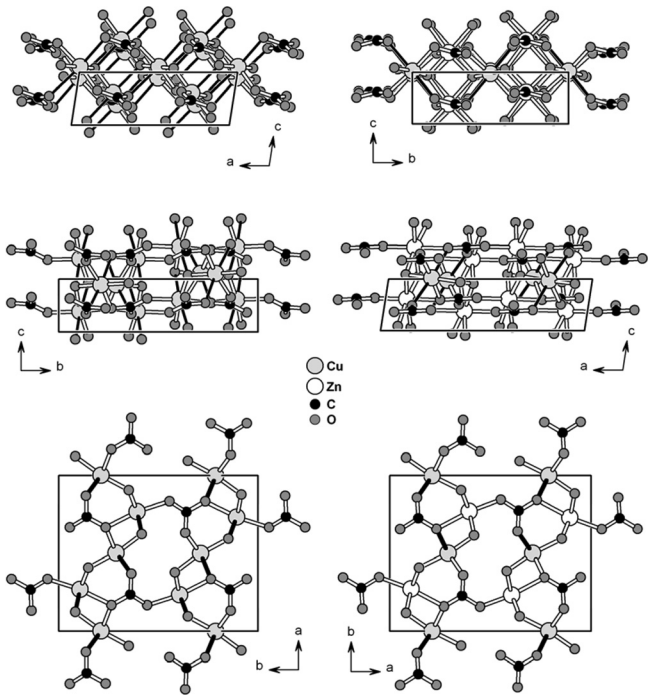

Figure 8. Correlation between the orientation of the Jahn–Teller elongated Cu–O bonds (emphasized in black) and the direction of the monoclinic distortion of the unit cell for malachite (left) and rosasite (right), viewed along the long (top row), middle (center row) and short (bottom row) unit cell axes.

ular zig-zag arrangement in rosasite. Conversely, when viewed along the medium axes (center row), they are almost parallel in rosasite and a little staggered in malachite, still being far away from a rectangular arrangement. At low Cu:Zn ratios, i.e. if the Jahn–Teller distorted units are diluted, the perpendicular zig-zig arrangement (rosasite structure) seems to be favorable, whereas at high Cu:Zn rations, i.e. if the Jahn–Teller distortions are concentrated, a more parallel orientation seems to be more stable resulting in the malachite structure. Thus, the hypothetical $Zn_2(OH)_2CO_3$ phase helps to understand the existence of different non-isomorphous structures for malachite and rosasite despite their similar composition and crystallization in the same class of space groups. In this context, the projections in Figure 8 are very suggestive, as it appears that the different monoclinic distortion in both minerals can be explained by the direction of parallel orientation of the projected Jahn–Teller elongations opening the respective angle to > 90° (top row, left and center row right). Finally, the differences of the malachite and rosasite structures can also be seen in the view along the short axis if the elongated bonds are considered (bottom row). In rosasite, the Jahn–Teller elongated bonds of $(M1)O_6$ point to the same carbonate ligand, whereas for malachite there is only one black bond per carbonate anion.

Whereas the XRD pattern of our mineral malachite sample could be fitted easily (Table 1, Figure 1), we encountered problems in the attempt to refine the rosasite structure. Due to anisotroptic peak broadening, no satisfying agreement of calculated and experimental pattern could be obtained. Furthermore, preliminary results using only the rosasite structure suggested presence of an additional phase since it could not account for two weak reflections at 31.9 and 32.9°2θ, which were already mentioned in [2] and are marked in Figure 1b. The fit became significantly better, though still not good enough for a reliable refinement of the atomic positions, when an additional (zincian) malachite phase was introduced as has been suggested in [2]. In Figure 1b only the resulting peak positions of such two phase fit are shown and the corresponding cell parameters are given in Table 1, showing that it is possible to have a mixture of the zincian malachite and rosasite phases, in which most of the well-resolved and intense XRD reflections overlap resulting in complex peak profiles. The $(20\bar{1})$ and $(21\bar{1})$ peaks of malachite are the striking exception among the intense reflections and the most obvious indication of the malachite-like phase fraction. It either is present as a separated impurity phase or as domains in the rosasite crystals resulting from fluctuations of the zinc content. On the basis of the linear trends shown in Figure 6, the zinc content x of this fraction of the mineral sample can be estimated to ca. 0.18 falling clearly below the average value of 0.38 determined by EDX. It is noted, though, that the scattering among the individual lattice constant was in the range $0.13 < x < 0.25$.

As a complementary technique, optical absorption spectroscopy was applied for natural as well as synthetic samples with nominal zinc contents of $x = 0$, 0.1 and 0.3. The spectra are shown in Figure 9. As expected, those of natural and synthetic malachite are similar. For malachite two major contributions are observed, an intensive band centered around 810 nm and a shoulder at lower energies near 1150 nm. These are typical features of tetragonally distorted octahedral CuO_6 chromophores [15–17]. Significant changes can be observed as the zinc content of the samples is increased. The subtle change of the color of the samples from green to bluish green is caused by a slight blue-shift of the former band into the vis-range of the spectrum and development of a shoulder at high energy seen most clearly in the spectrum of rosasite (indicated by an arrow in Figure 9). However, the changes are much more pronounced at lower energy in the NIR. This spectral range was reported to be suitable for discrimination of rosasite group minerals [18]. The band at 1150 nm was assigned to the $^2B_{1g} \rightarrow {}^2A_{1g}$ transition of Cu^{2+} [18] and its relative intensity decreases as copper is substituted by optically silent Zn^{2+}. The band is also shifted to lower energies, which may be associated with the geometrical effect of the Zn^{2+} ions on the MO_6 polyhedra as shown above in Figure 6e affecting also the CuO_6 chromophores. The rough correlation of the position of this band with the zinc content (Figure 10) renders optical spectroscopy in the range > 1000 nm an alternative tool for convenient estimation of the Cu:Zn ratio in zincian malachite, which is not affected by the crystallographic differences of malachite and rosasite.

In summary, these results suggest a relative phase stability of mixed Cu,Zn basic carbonates as shown in the simplified free energy diagram in Figure 11. At $x = 0$, malachite is the most stable phase and synthetically easily accessible. As x increases low amount of copper in malachite can be substituted

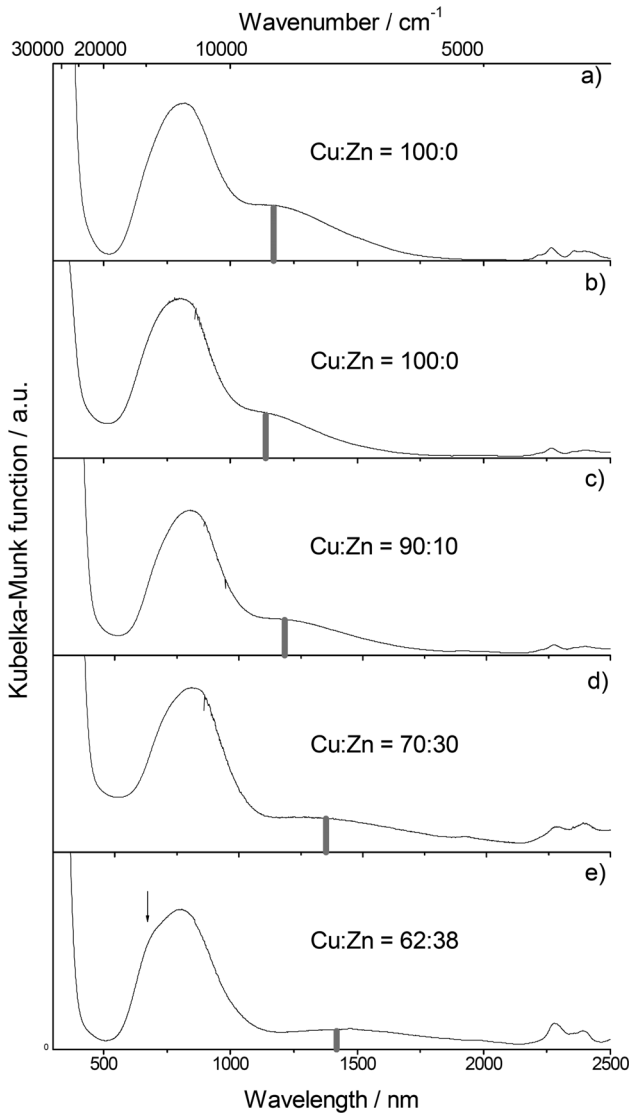

Figure 9. Optical absorption spectra in the UV/Vis/NIR range of the minerals malachite (a) and rosasite (e) and of the synthetic zincian malachite samples with 100 % (b), 90 % (c), and 70 % copper (d). The grey bars mark the position of the low-energy band determined from a simple fit the range 500–2100 nm with two Gaussians.

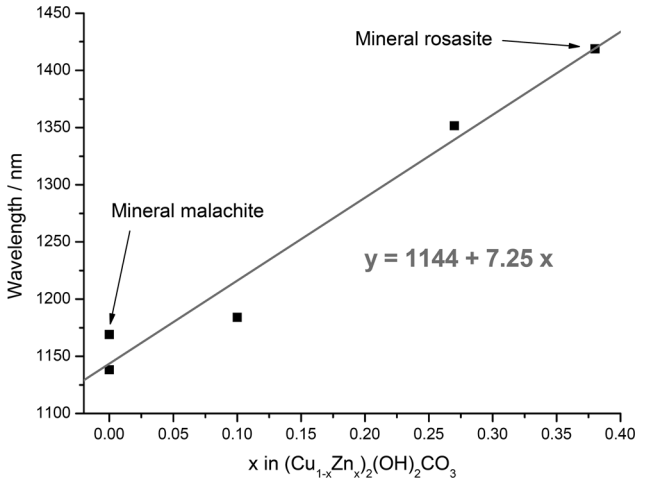

Figure 10. Position of the low energy band on the wavelength-scale in the optical absorption spectra of $(Cu_{1-x}Zn_x)_2(OH)_2CO_3$ samples as a function of zinc content. The contribution of the minor amount of by-phases in the two Zn-richest samples (see text) has been neglected.

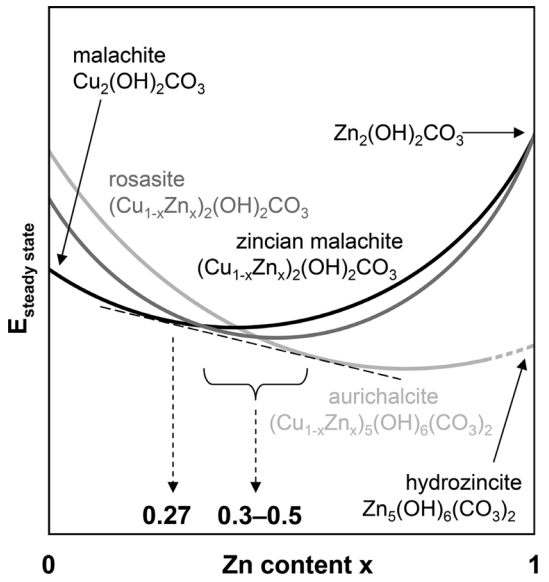

Figure 11. Proposed energetic situation of the basic carbonate systems $(Cu_{1-x}Zn_x)(OH)_2CO_3$ and $(Cu_{1-x}Zn_x)_5(OH)_6(CO_3)_2$, which are important in the context of Cu/ZnO catalyst synthesis. This representation is strongly idealized and neglects, e.g., differences in anion composition.

by zinc leading to zincian malachite (black curve in Figure 11). At a critical composition, no more zinc can be incorporated into zincian malachite and formation of a phase mixture of zincian malachite and aurichalcite is energetically favorable. The reason is most probably the increasing concentration of regular MO_6 octahedra, which destabilizes the aligned arrangement of the Jahn–Teller distortions present in malachite. Aurichalcite (light grey curve) exhibits a higher variability of building units [19], e.g. also tetrahedrally coordinated and almost undistorted octahedral sites are available, which can accommodate zinc ions [20].

Under the synthesis conditions applied for this study the critical composition is at $x = 0.27$ and the two-phase regime lasts until x ca. 0.5 [21]. It is noted that these values strongly depend on the exact setting of the synthesis conditions like pH, temperature and ageing time, but also on the general mode of co-precipitation. For instance, if the decreasing pH technique is used at otherwise the same conditions, the critical composition cannot exceed $x = 0.11$ [2] and the two-phase regime ends at approximately $x = 0.60$ [21]. Thus, the relative positions of the curves in Figure 11, which were chosen to qualitatively agree with thermodynamical data reported in literature [22], are a function of the synthesis parameters indicating that the applied method of preparation does not necessarily lead to equilibrium phases.

Rosasite seems to be metastable towards zincian malachite and/or aurichalcite at all compositions (dark grey curve) as it

is not accessible by the coprecipitation and ageing procedure. According to the above considerations the curves of zincian malachite and rosasite should meet at $x = 1$, the hypothetical common $Zn_2(OH)_2CO_3$ phase. Anyway, rosasite is accessible under naturally occurring mineralization conditions for compositions $0.3 < x < 0.5$.

Consequences of the situation depicted in Figure 11 for preparation and optimization of Cu/ZnO catalysts relate to the observation that a coarse relationship between the zinc content x in $(Cu_{1-x}Zn_x)(OH)_2CO_3$ and the catalytic activity of the resulting Cu/ZnO catalyst exists [6]. Near the critical limit of 0.27 a maximum of gas accessible copper surface areas, i.e. highest dispersion of copper, was observed due to an efficient nanostructuring of the precursor upon thermal treatment (Figure 2). At $x > 0.27$, aurichalcite is formed as a by-phase and the decreasing catalytic activity is attributed to the unfavorable *meso*-structure of this precursor phase leading to undesired embedment of the active copper particles. Thus, synthesis conditions have to be found, which either drive the critical composition of zincian malachite beyond $x = 0.27$ by lowering the black curve or make rosasite-like precursors accessible by lowering the dark grey curve.

Conclusions

The main conclusions of this work are: (i) Malachite and rosasite, $(Cu_{1-x}Zn_x)(OH)_2CO_3$, which are not boundary cases of an isomorphous substitution series [4], can be envisaged as two alternative distortions of a hypothetical common orthorhombic parent structure as a function of Cu:Zn ratio. Synthetic samples with a zinc content of up to $x = 0.27$ adopt the malachite-like structure, which exhibits a more coaxial arrangement of the Jahn–Teller distorted polyhedra and, thus, seems not to be able to incorporate larger amounts of preferably symmetrically coordinated Zn^{2+} ions. (iii) As expected, zinc preferably occupies the less distorted *M*2 site in synthetic zincian malachite and Cu-Zn substitution leads to anisotropic, but linear Vegard-type changes of the malachite lattice constants, which due to a compensating effect are hardly reflected in the peak positions of most XRD reflections. (iii) In natural samples both phases may coexist, possibly as domains with different zinc contents. This phase coexistence may be difficult to see by powder XRD, because the individual patterns are very similar and differ only in a few selected reflections. (iv) In addition to full pattern refinement or analysis of the d-spacing of the characteristic $(20\bar{0})$ or $(21\bar{1})$ peaks [2], optical spectroscopy can be applied to estimate the Cu:Zn ratio in zincian malachite catalyst precursors.

Experimental Section

Mineral samples were obtained from the mineral collection of the Technical University Berlin. Elemental analyses by EDX revealed a zinc content x of 0.38 for the rosasite sample [2]. In case of malachite, EDX showed that in the mineral sample 7 % of the cations were Al^{3+} or Si^{4+}, which are probably present in an impurity phase not seen by XRD. However, another 2 % are Mg^{2+}, which could possibly reside on the copper sites in the malachite structure. Further analyses of the minerals like TG and IR spectroscopic investigations can be found in [2]. The series of synthetic zincian malachite samples was prepared with varying molar Cu/Zn ratios of 100:0, 90:10, 80:20 and 70:30 by constant-pH coprecipitation and some results were presented in earlier contributions [2, 6, 21]. Coprecipitates were obtained by cofeeding mixed metal nitrate and soda solutions at pH 7 and $T = 65$ °C. The initially amorphous precipitates (zincian georgeite [23]) were aged in the mother liquor for 2 h. During ageing crystallization occurred and the solids were recovered by filtration, washing and drying. Further details on the preparation process can be found in ref. [21] and [6].

For the synthetic samples, the X-ray diffraction (XRD) measurements were performed with a STOE STADI P transmission diffractometer equipped with a primary focusing germanium monochromator (Cu-$K_{\alpha1}$ radiation) and a curved position sensitive detector (static mode, resolution 0.03°, accumulation time 1800 s). The sample powders were filled into 0.3 mm diameter glass capillaries and mounted on a capillary sample holder, which was rotated around the capillary axis during measurement. The mineral samples were measured on the same setup, except that a linear position sensitive detector was used (moving mode, step size 0.1°, counting time 10 s per step, resolution 0.01°, total accumulation time 634 s) and the samples were mounted in the form of a clamped sandwich of small amounts of powder fixed with a small amount of grease between two layers of thin polyacetate film. Refinements were done in the 2θ range 5–90° using the software package TOPAS [24]. Only 2θ-sections of 10–50° are shown in the figures for clarity. The background for the mineral samples was modelled using a third order Chebychev polynomial, whereas the synthetic samples required a second order Chebychev polynomial plus a very broad (FWHM > 5° 2θ) Gaussian peak around 25–30° 2θ to account for the diffuse scattering caused by the glass capillary walls. Details of the refinements are given in Table 3.

Table 3. Technical details of the Rietveld refinements.

	$x = 0$	$x = 0.1$	$x = 0.2$	$x \approx 0.27$	malachite (mineral)
R_{exp} a)	0.0158	0.0164	0.0150	0.0152	0.0753
R_{wp} a)	0.0406	0.0265	0.0256	0.0264	0.0920
R_p a)	0.0308	0.0209	0.0204	0.0207	0.0689
R_{exp}' a)	0.0361	0.0574	0.0352	0.0399	0.1701
R_{wp}' a)	0.0928	0.0932	0.0602	0.0696	0.2079
R_p' a)	0.0813	0.0867	0.0547	0.0609	0.2152
GOF	2.57	1.62	1.71	1.74	1.22
R_{Bragg}	0.01060	0.00846	0.00452	0.00561	0.02989
No. of reflections	225	224	222	221	226
No. of parameters	57	57	57	39	51

a) Primed *R* values are background corrected; definition of the *R* values according to [26].

Diffuse reflectance UV/Vis–NIR spectroscopy was performed using a PerkinElmer Lambda 950 spectrometer equipped with a Harrick Praying Mantis DRP-P72 accessory and HVC-VUV reaction chamber. The spectra of selected samples were measured in the spectral range 250–2500 nm at room temperature in static air. For the background correction the Spectralon reflectance standard (Labsphere) was used. All spectroscopic measurements were carried out sequentially with a scan speed of 266 nm·min^{-1}, a nominal slit width of 2.5 nm, a response time of 0.20 s, and a step width of 1 nm. The apparent absorption

Zeitschrift für anorganische und allgemeine Chemie ZAAC Journal of Inorganic and General Chemistry

$K(\lambda)$ as a function of the wavelength λ was evaluated from the diffuse reflectance data using the Kubelka-Munk equation.

Acknowledgement

We thank *Nicole Giliard* and the *Technical University, Berlin* for providing the mineral reference samples, *Edith Kitzelmann* for XRD measurements, *Gisela Weinberg* for EDX analyses and *Genka Tzolova-Müller* for recording the optical spectra. *Sophia Klokishner*, *Oleg Reu*, *Igor Kasatkin*, *Annette Trunschke* and *Robert Glaum* are acknowledged for fruitful discussion of the spectroscopic results. Financial support was given by the *BMBF* (Förderkennzeichen 01RI0529). *Robert Schlögl* is greatly acknowledged for his continuous support.

References

[1] F. Zigan, W. Josig, H. D. Schuster, *Z. Kristallogr.* **1977**, *145*, 412.
[2] M. Behrens, F. Girgsdies, A. Trunschke, R. Schlögl, *Eur. J. Inorg. Chem.* **2009**, *10*, 1347.
[3] A. C. Roberts, J. L. Jambor, J. D. Grice, *Powd. Diff.* **1986**, *1*, 56.
[4] N. Perchiazzi, *Z. Kristallogr. Suppl.* **2006**, *23*, 505.
[5] N. Perchiazzi, S. Merlino, *Eur. J. Mineral.* **2006**, *18*, 787.
[6] M. Behrens, *J. Catal.* **2009**, *267*, 24.
[7] D. Waller, D. Stirling, F. S. Stone, M. S. Spencer, *Faraday Discuss. Chem. Soc.* **1989**, *87*, 107.
[8] T. Fujitani, J. Nakamura, *Catal. Lett.* **1998**, *56*, 119.
[9] R. G. Herman, K. Klier, G. W. Simmons, B. P. Finn, J. B. Bulko, T. P. Kobylinski, *J. Catal.* **1979**, *56*, 437.
[10] P. Porta, G. Fierro, M. Lo Jancono, G. Moretti, *Catal. Today* **1988**, *2*, 675.
[11] P. Porta, S. De Rossi, G. Ferraris, M. Lo Jacono, G. Minelli, G. Moretti, *J. Catal.* **1988**, *109*, 367.
[12] S. Schimpf, M. Muhler, in: *Synthesis of Solid Catalysts* (Ed.: K. P. de Jong), Wiley-VCH, Weinheim, **2009**,pp. 329 ff.
[13] R. K. Eby, F. C. Hawthorne, *Acta Crystallogr., Sect. B* **1993**, *49*, 28.
[14] I. V. Pekov, N. Perchiazzi, S. Merlino, V. N. Kalachev, M. Merlini, A. E. Zadov, *Eur. J. Mineral.* **2007**, *19*, 891.
[15] B. J. Hathaway, D. E. Billing, *Coord. Chem. Rev.* **1970**, *5*, 143.
[16] K. M. Reddy, A. S. Jacobs, B. J. Reddy, Y. P. Reddy, *Phys. Status Solidi* **1987**, *B139*, K145.
[17] R. Glaum, M. Weil, D. Özalp, *Z. Anorg. Allg. Chem.* **1996**, *622*, 1839.
[18] R. L. Frost, B. J. Reddy, D. L. Wain, W. N. Martens, *Spectrochim. Acta* **2007**, *A66*, 1075.
[19] M. M. Harding, B. M. Kaiuki, R. Cernik, G. Cressey, *Acta Crystallogr., Sect. B* **1994**, *50*, 673.
[20] J. M. Charnock, P. F. Schofield, C. M. B. Henderson, G. Cressey, B. A. Cressey, *Mineral. Magn.* **1996**, *60*, 887.
[21] B. Bems, M. Schur, A. Dassenoy, H. Junkes, D. Herein, R. Schlögl, *Chem. Eur. J.* **2003**, *9*, 2039.
[22] A. K. Alwan, J. H. Thomas, P. A. Wiliams, *Trans. Met. Chem.* **1980**, *5*, 3.
[23] A. M. Pollard, M. S. Spencer, R. G. Thomas, P. A. Williams, J. Holt, J. R. Jennings, *Appl. Catal. A* **1992**, *85*, 1.
[24] A. A. Coelho, *Topas*, General Profile and Structure Analysis Software for Powder Diffraction Data, Version 3.0, Bruker AXS GmbH, Karlsruhe, Germany, **2006**.
[25] I. Kasatkin, P. Kurr, B. Kniep, A. Trunschke, R. Schlögl, *Angew. Chem.* **2007**, *119*, 7465.
[26] R. A. Young in: *The Rietveld Method* (Ed.: R. A. Young), Oxford University Press **1993**,pp. 1 ff.

Received: January 12, 2010
Published Online: April 8, 2010

